Materials and Design 196 (2020) 109083

Contents lists available at ScienceDirect

Materials and Design

journal homepage: www.elsevier.com/locate/matdes

Growth and characterization of novel $Ir_{1-x}Cr_xO_2$ thin films

E. Arias-Egido [a,b], M.A. Laguna-Marco [a,b,*], C. Piquer [a,b], J. Chaboy [b], G. Fabbris [c], D. Haskel [c]

[a] Instituto de Ciencia de Materiales de Aragón, CSIC – Universidad de Zaragoza, 50009, Spain
[b] Departamento de Física de la Materia Condensada, Universidad de Zaragoza, Zaragoza 50009, Spain
[c] Advanced Photon Source, Argonne National Laboratory, Argonne, IL 60439, USA

GRAPHICAL ABSTRACT

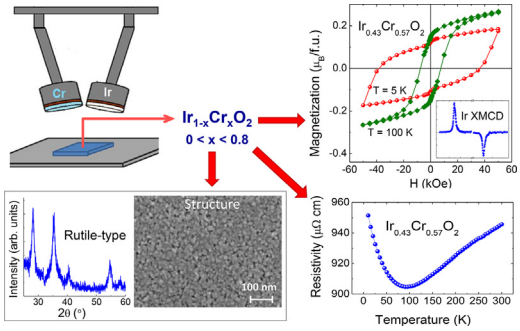

ARTICLE INFO

Article history:
Received 4 June 2020
Received in revised form 19 August 2020
Accepted 21 August 2020
Available online xxxx

Keywords:
Magnetic thin films
XMCD
Spintronics
Transition metal oxides
Spin–orbit coupling

ABSTRACT

Novel $Ir_{1-x}Cr_xO_2$ thin films have been prepared by reactive co–sputtering deposition. Composition, structure and electric and magnetic behavior have been analyzed by different techniques including EDX, XRR, XRD, SQUID magnetometry, electrical resistivity and XANES and XMCD spectroscopies. Despite the difficulty in growing CrO_2 by physical deposition techniques, an $Ir_{1-x}Cr_xO_2$ solid solution phase could be achieved for $0 \le x \le 0.8$, where the oxidation state of Cr is found to remain as 4+. Both the electrical and the magnetic behavior are shown to starkly depart from those of the parent IrO_2 (paramagnetic metal) and CrO_2 (half–metal ferromagnet) compounds. In particular, they show a semiconducting behavior, $d\rho/dT < 0$ and giant magnetic coercivity at low temperatures. XMCD reveals a significant contribution of Ir to the magnetic response of the $Ir_{1-x}Cr_xO_2$ films. In addition, the nature of the magnetic moment of the Ir^{4+} ion ($\langle m_l \rangle / \langle m_s \rangle = 0.09$) is completely different from the large orbital moment that is a hallmark of insulating Ir^{4+} oxides. This suggests a Cr–induced magnetic moment, which is a remarkably surprising result for an oxide.

1. Introduction

CrO_2 is a half–metallic ferromagnetic material with a high ordering temperature (T_C in the 385–400 K range), very small coercive field (< 100 Oe) and a magnetic moment of 2 μ_B/Cr [1–4]. By virtue of these properties, it is extensively explored for the development of new spintronic devices, [5–10]. However, CrO_2 is a metastable rutile phase with a tendency to decompose into the insulating antiferromagnetic and more stable Cr_2O_3 phase under atmospheric conditions [4,11]. In addition, conventional film growing techniques such as sputtering or pulsed laser deposition have not succeeded in synthesizing this compound. So far, only chemical methods such as thermal decomposition and chemical vapor deposition have been successful in depositing CrO_2 thin films [12,13]. In this context and given the practical importance of sputtering techniques to grow films in favorable

* Corresponding author at: Instituto de Ciencia de Materiales de Aragón, CSIC – Universidad de Zaragoza, 50009, Spain.
E-mail address: anlaguna@unizar.es (M.A. Laguna-Marco).

https://doi.org/10.1016/j.matdes.2020.109083

industrial production conditions, developing alternative routes to make CrO_2 or CrO_2–related films is an objective of undoubtable interest.

Within this context in this work the growth of novel $Ir_{1-x}Cr_xO_2$ phases has been explored. Chemical doping as an alternative route to stabilize Cr^{4+} in the rutile form has been barely and only recently explored [14,15]. Regarding Ir-doping, neither the synthesis of bulk nor the growth of thin films of $Ir_{1-x}Cr_xO_2$ has been reported to date. However, the formation of stable $Ir_{1-x}Cr_xO_2$ compounds can be expected since both IrO_2 and CrO_2 crystallize in the same space group with similar lattice parameters and Cr and Ir conform to the Hume–Rothery rules for the formation of a substitutional solid solution phase. Moreover, Ir is the optimal candidate to stabilize Cr in the rutile structure as IrO_2 is the only stable solid IrO_x compound.

Additionally, the relevance of using Ir is two-fold. First, the introduction of high spin–orbit coupling (SOC) Ir ions allows taking benefit of the spin Hall effect (SHE) or anomalous Hall effect (AHE) so these systems become potential candidate materials for spin–current manipulation as source/detector of spin currents [16]. The combination of the half-metal properties of CrO_2 and the high SOC of IrO_2 in a single material could even provide access to the design of innovative properties. Secondly, the use of Ir ions may lead to the control of the magnetic anisotropy (MA) [17–21]. In fact, huge coercivity (up to 550 kOe) has been reported on iridium oxides such as $BaIrO_3$ and Sr_3NiIrO_6 [22,23]. Compared to the localized 4*f* states where magnetism resides in rare earths elements, the large spatial extension of the 5*d* orbitals in iridium may prove to be more efficient in inducing hardness on the neighboring 3*d*–transition metal. Adjusting the amount of Ir doping is proposed as a route to the fabrication of thin films with tunable controlled magnetic coercivity. From an applied point of view, magnetic materials with large coercivity have broad applications ranging from permanent magnets and data storage media to high–frequency electromagnetic wave filters [24,25].

Moreover, combining IrO_2 and CrO_2 is an interesting approach, not only for growing and tuning the magnetic properties of CrO_2, but also for manipulating the magnetism of IrO_2, one of the most promising materials for spin–current detection [26]. Indeed, while IrO_2 is found to be a metallic paramagnet, several theoretical studies have predicted that such ground state can be tuned through structural modifications [27–29].

Finally, the $Ir_{1-x}Cr_xO_2$ systems may be interesting materials also in the field of electrocatalysis. Electrochemical water splitting is promising for utilizing intermittent renewable energy and nowadays IrO_2-based systems, such as IrO_2-TiO_2 and IrO_2— RuO_2, are widely studied for the development of more efficient water electrolyzers [30,31]. Taking into account all the possible oxidation states of both Ir and Cr, $Ir_{1-x}Cr_xO_2$ oxides may be proposed promising candidates for the design of more efficient electrolyzers.

Considering the potential impact that IrO_2–CrO_2 systems can have in spintronics and in the development of new permanent magnets, it is surprising that no studies have been reported on this system. Aimed at exploring this new playground a first work is presented here where sputtered $Ir_{1-x}Cr_xO_2$ thin films have been successfully fabricated and structurally, electrically and magnetically characterized.

2. Method

$Ir_{1-x}Cr_xO_2$ thin films were prepared by reactive magnetron co–sputtering deposition on Si substrates at room temperature (RT) from metallic Ir and Cr targets connected to a DC and a pulsed DC source, respectively. The power supplied to the Ir target was set to ~8 W while for the Cr target the sputtering power was varied from 15 to 198 W to obtain dilutions with different Ir/Cr ratio, ranging from 10 to 80 at.% Cr. The gas flows were set to 13 ml Ar/min and 2 ml O_2/min. Finally, the amorphous as–grown films were subsequently annealed in air at 600 °C during 6 h to obtain polycrystalline samples. Pure IrO_2, grown by the same sputtering process, and pure epitaxial CrO_2 [3] films, grown by chemical vapor deposition, were used as references.

The composition of the films was determined by Energy Dispersive X–Ray Spectroscopy (EDX) measurements performed in an INSPECT 50 FE–SEM working at 10 kV (highest–energy principal line is Ir L_α at ~9 keV). X–ray reflectivity (XRR) and X–ray diffraction (XRD) measurements were performed on a Bruker D8 X–ray diffractometer by using the Kα radiation line of copper. The resistivity measurements were carried out in a PPMS 9 T and the magnetic measurements in a SQUID magnetometer MPMS–5 T (both from Quantum Design).

X–ray absorption near edge structure spectroscopy (XANES) and X–ray magnetic circular dichroism (XMCD) measurements were carried out at the 4–ID–D beamline of the Advanced Photon Source at the Argonne National Laboratory. Partial fluorescence yield spectra were recorded at the Ir $L_{2,3}$ edges and the Cr K edge at 10 K using a 4–element silicon drift diode detector. XMCD was measured in helicity–switching mode for two directions of the applied magnetic field (5 T) along and opposite to the incident photon wave vector to remove spurious signals. Undulator radiation was monochromatized with double Si(111) crystals and its polarization converted from linear to circular with a diamond quarter–wave plate operated in Bragg transmission geometry. The computation of the XANES spectra was carried out using the multiple–scattering code CONTINUUM [32] now included in the MXAN package [33]. A complete discussion of the procedure can be found elsewhere [34].

3. Results and discussions

As summarized in Table 1, thin films with ~80 nm thickness and evenly–spaced Cr content in the ~10–80 at.% Cr range have been grown. Fig. 1(a) shows that all the $Ir_{1-x}Cr_xO_2$ films exhibit a polycrystalline non–textured microstructure and crystallize in the rutile–type structure ($P4_2/mnm$ space group). As the Cr content increases, the Bragg peaks position progressively shifts from those of IrO_2 to those of CrO_2. Diffraction peaks corresponding to pure IrO_2 or CrO_2 phases are not discerned in any sample, *i.e.*, phase separation is not observed. Moreover, the peak width indicates a roughly constant grain size of around 9 nm (as derived from Scherrer equation) regardless of the Cr content. On the other hand, for $x \geq 0.6$ the diffraction peaks become less intense. The fact that the peak width is roughly constant and its intensity decreases with the Cr content, suggests the coexistence of differentiated crystalline and amorphous regions, with greater relative weight of the latter as the Cr content is increased. Indeed, in the sample with the highest Cr content, $x = 0.77$, the XRD pattern indicates a mostly amorphous phase. The reason for the increase of amorphous regions as we approach CrO_2 is rooted in the fact that IrO_2 films can be easily deposited by magnetron sputtering while CrO_2 cannot.

The calculated lattice parameters from Rietveld analyses are included in Table 1 along with the cell volume. A nearly linear decrease of the cell volume with the Cr doping is obtained (see Fig. 1(b)). Therefore, the XRD measurements indicate that, when sputtered in an O_2–

Table 1
Structural and compositional properties of $Ir_{1-x}Cr_xO_2$ thin films: layer thickness (t) measured by XRR and Cr concentration determined by EDX (relative to the total Ir + Cr content). Lattice parameters obtained from XRD and cell volume.

Sample	t (nm)	Cr (%) (±2%)	$a = b$ (Å)	c (Å)	Cell Vol. (Å^3)
$Ir_{0.86}Cr_{0.14}O_2$	89	14	4.482(5)	3.118(4)	62.6(1)
$Ir_{0.75}Cr_{0.25}O_2$	89	25	4.488(5)	3.106(4)	62.5(1)
$Ir_{0.67}Cr_{0.33}O_2$	90	33	4.482(6)	3.091(5)	62.1(2)
$Ir_{0.54}Cr_{0.46}O_2$	90	46	4.466(6)	3.059(4)	61.0(1)
$Ir_{0.43}Cr_{0.57}O_2$	83	57	4.472(8)	3.056(8)	61.1(2)
$Ir_{0.32}Cr_{0.68}O_2$	71	68	4.42(1)	3.00(1)	58.6(4)
$Ir_{0.23}Cr_{0.77}O_2$	71	77	4.42(3)	2.98(3)	58.2(8)

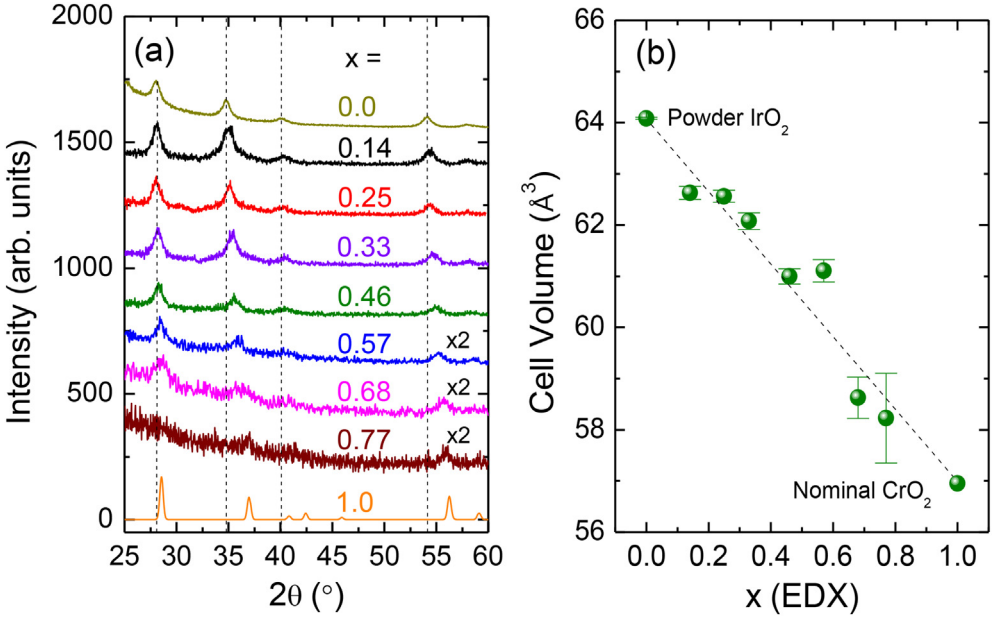

Fig. 1. (a) XRD patterns for annealed $Ir_{1-x}Cr_xO_2$ thin films. A simulated pattern of polycrystalline pure CrO_2 ($x = 1$) is included as a reference. The dashed lines mark the position of the diffraction peaks measured on IrO_2. (b) Dependence of the cell volume with the Cr–concentration obtained from EDX experiments. The dotted line is a guide to the eye.

rich atmosphere, Ir and Cr form a $Ir_{1-x}Cr_xO_2$ substitutional solid solution phase.

The unit cell contraction observed with Cr doping is found to be remarkably large, up to ~10% in the $Ir_{0.28}Cr_{0.77}O_2$ sample respect to pure IrO_2. Such contraction is rooted in the smaller size of the Cr^{4+} ionic radius (0.55 Å) relative to Ir^{4+} (0.625 Å). Nevertheless, a concomitant reduction of the IrO_6 octahedra may also be expected. In this sense, it is worth noticing that the rutile structure, with edge–sharing octahedra, is quite rigid (compared for instance to perovskites) and not as susceptible to distortion *via* inter–octahedral M–O–M tilting (M = Ir, Cr).

The XANES spectra recorded at the Ir $L_{2,3}$ edges and Cr K edge provide information about the SOC and the oxidation state of Ir and Cr. Practically identical XANES profiles are obtained for $Ir_{0.43}Cr_{0.57}O_2$ and IrO_2 films (Fig. 2(a)). This indicates a similar ground–state expectation value of the angular part of the SOC, $\langle \mathbf{L}\cdot\mathbf{S}\rangle$, which is found to be 2.0 (in units of $\hbar^2$) [35,36]. Although more samples of the series should be measured, it seems reasonable to affirm that all the $Ir_{1-x}Cr_xO_2$ dilutions remain in a high SOC regime. A similar conclusion was reached for Rh–doped Sr_2IrO_4 [37].

Fig. 2 also shows that the spectrum of the $Ir_{0.43}Cr_{0.57}O_2$ sample is slightly shifted (~0.3 eV) to higher energies with respect to pure IrO_2. Upon reducing the first neighboring interatomic distance of the absorbing atom a shift in the absorption threshold towards higher energies is expected. Therefore, the experimentally observed shift suggests smaller Ir—O distances as Cr is incorporated in the IrO_2 framework. This is in agreement with the gradual reduction of the size of the lattice induced by Cr doping, observed in the XRD diffractograms.

As for the XANES spectra recorded at the Cr K edge (Fig. 2(b)), some notable differences can be observed between the spectra of $Ir_{0.43}Cr_{0.57}O_2$ and CrO_2 films. The amplitude and width of the XANES oscillations are modified. Besides, regarding the near–edge region, the $Ir_{0.43}Cr_{0.57}O_2$ film presents a broader shoulder–like feature at ~6003 eV and the raising edge looks somehow less sharp. As a result, in some parts of the threshold a small shift of ~0.6 eV towards lower energies is observed.

As in the Ir case, the change in the XANES profile can be explained in terms of Cr—O distances, as confirmed by XANES calculations. Fig. 3 (a) shows the calculations corresponding to CrO_2 and $Ir_{0.43}Cr_{0.57}O_2$. In the latter case, for the sake of simplicity, the $Ir_{0.5}Cr_{0.5}O_2$ stoichiometry,

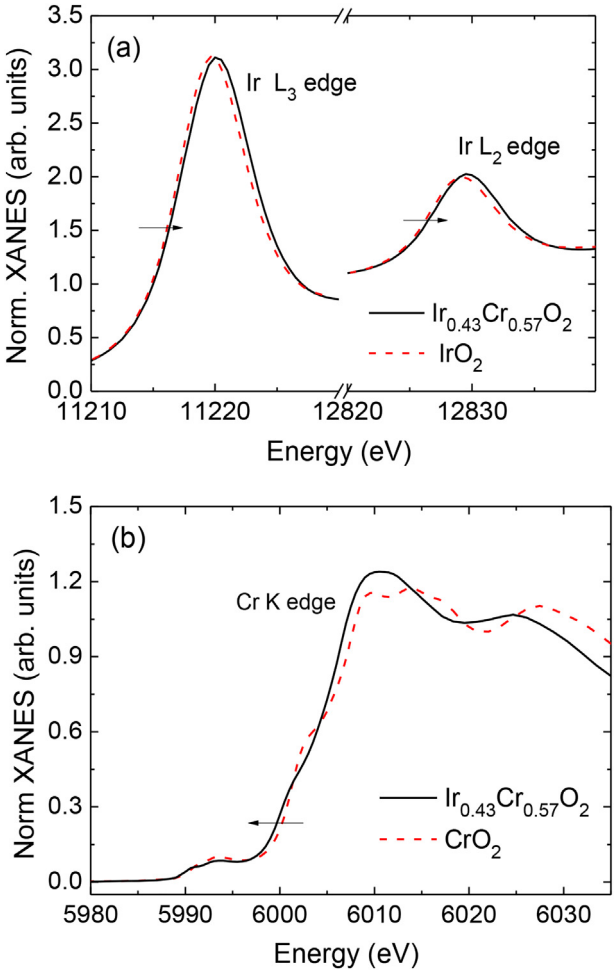

Fig. 2. Normalized (a) Ir $L_{2,3}$–edges and (b) Cr K–edge XANES spectra recorded at 10 K on the $Ir_{0.43}Cr_{0.57}O_2$ sample accordingly compared to those of pure IrO_2 and CrO_2 films.

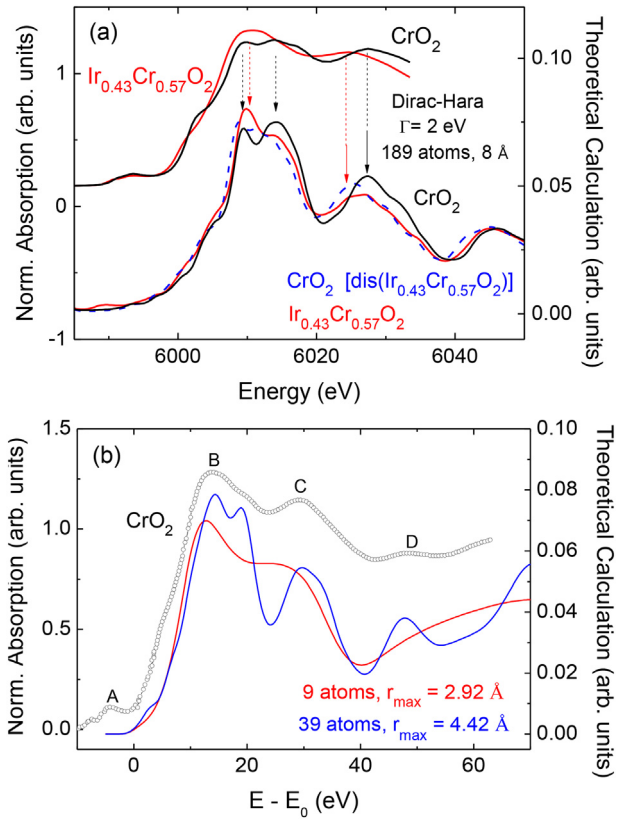

Fig. 3. (a) Normalized Cr K–edge XANES spectra of the $Ir_{0.43}Cr_{0.57}O_2$ and pure CrO_2 films compared to the theoretical spectra of CrO_2, $Ir_{0.43}Cr_{0.57}O_2$ and CrO_2 with the atomic distances of $Ir_{0.43}Cr_{0.57}O_2$. In panel (b) the effect of disorder is illustrated by simulating two different cluster sizes (9 and 39 neighbors) compared with a CrO_2 reference.

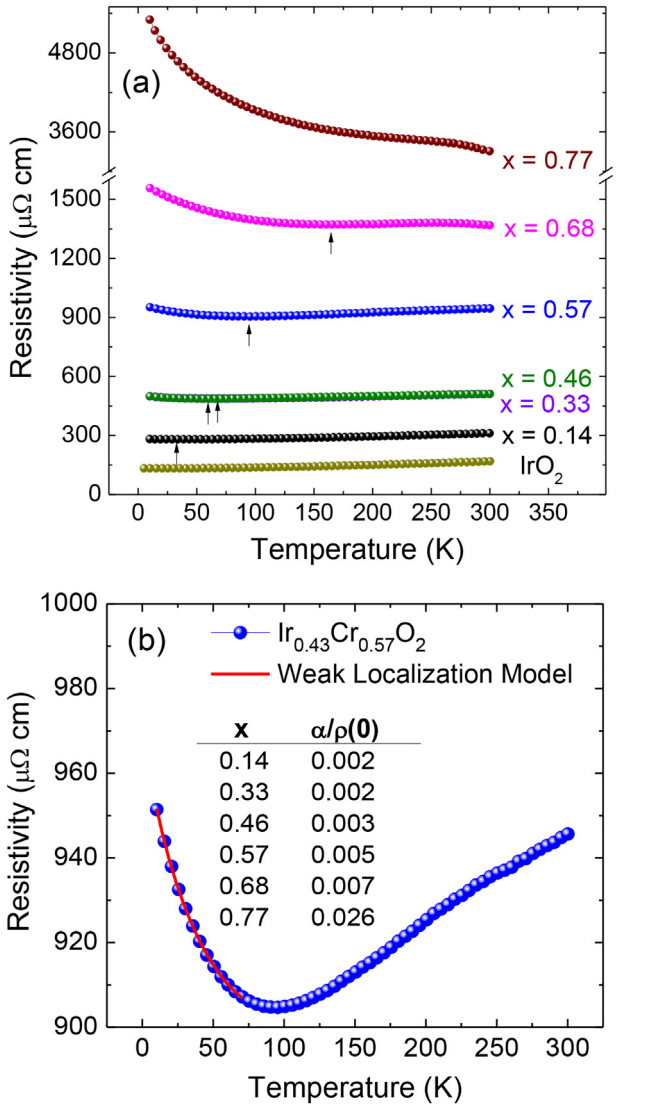

Fig. 4. (a) ρ(T) curves measured in the annealed $Ir_{1-x}Cr_xO_2$ films. (b) ρ(T) curve of the representative $Ir_{0.43}Cr_{0.57}O_2$ sample fitted to a weak localization model. The table gives the $\alpha/\rho(0)$ values obtained from the fittings for each sample.

by substituting half of the Cr atoms in the cluster by Ir atoms in an alternating manner, has been used. Choosing different Ir—Cr substitution schemes slightly modifies the amplitude of the main peak, but the overall profile remains invariable. Moreover, calculations have been also performed for a CrO_2 cluster but imposing the interatomic distances of $Ir_{0.43}Cr_{0.57}O_2$. In addition, in Fig. 3(b) the profile calculated for two different clusters sizes of CrO_2 is displayed to illustrate the effect of disorder. As can be seen in Fig. 3(a), modifiying the Cr—O distances to those of (expanded) $Ir_{0.43}Cr_{0.57}O_2$ has an important effect on the profile. Indeed, the threshold is slightly shifted and the XANES oscillations are modified, so that the profile reproduces the experimental spectrum of the $Ir_{0.43}Cr_{0.57}O_2$ sample. From these simulations it is also established that both, the substitution of Cr by Ir and the increase of structural disorder have a smaller effect on the threshold. Nevertheless, their effect is in accordance with the observed experimental spectrum.

Being Cr_2O_3 the most stable Cr oxide, one might also propose the presence of Cr_2O_3. However, Cr_2O_3 has a 3+ oxidation state and presents a shift in the threshold energy around 3 eV towards lower energies respect to the spectrum of pure CrO_2 [38]. In consequence, the presence of a measurable amount of Cr^{3+} (Cr_2O_3–like) can be discarded. Therefore, it can be concluded that the Cr ions in the $Ir_{0.43}Cr_{0.57}O_2$ film are actually in a rutile crystal structure and present a 4+ oxidation state. This, in turn, confirms the 4+ oxidation state for Ir ions.

Regarding the electrical behavior, both CrO_2 and IrO_2 (bulk and films with $t \geq 50$ nm) present metallic behavior with resistivity ranging from ~10 μΩ cm at low temperature up to ~10^3 μΩ cm at room temperature [2,26,39] . Bearing this in mind, one would naively expect the $Ir_{1-x}Cr_xO_2$ films to be metallic regardless of the Cr content. However, the ρ(T) curves, displayed in Fig. 4(a), show the appearance of clear upturns (marked with arrows in the figure). Such upturns are observed at increasing temperatures as the Cr content is increased, up to $x = 0.77$, where $d\rho/dT < 0$ in the whole range of temperatures, *i.e.* the $Ir_{0.23}Cr_{0.77}O_2$ sample presents a semiconductor–like behavior.

From this behavior the presence of localization mechanism (s) hindering the movement of the electrons can be concluded. Analysis based on typical resistivity models, such as thermal activation or Mott–hopping, are not able to reproduce the electrical response observed in Fig. 4(a) (not shown). This fact suggests that neither correlations (Mott insulator) nor magnetism (Slater insulator) are responsible for the localization. On the other hand, the observed response is similar to that reported by J. H. Gruenewald et al. [40] in compressed $SrIrO_3$ thin films. In that work the metal–insulator transition (MIT) was attributed to weak localization, a disorder–driven effect due to quantum interference of the conducting charge carriers at defect sites [41]. Following that work, Fig. 4(b) illustrates that, in these films, the resistivity in the low temperature region is well fitted to the weak localization model $\rho = \rho(0) - \alpha T^{3/4} + \beta T^{3/2}$ [42], where $\rho(0)$, α, and β stand for the remnant resistance, three–dimensional weak localization, and inelastic scattering due to electron–boson interactions, respectively. Excellent fits are obtained in all the samples, giving increasing values of $\alpha/\rho(0)$ as the Cr

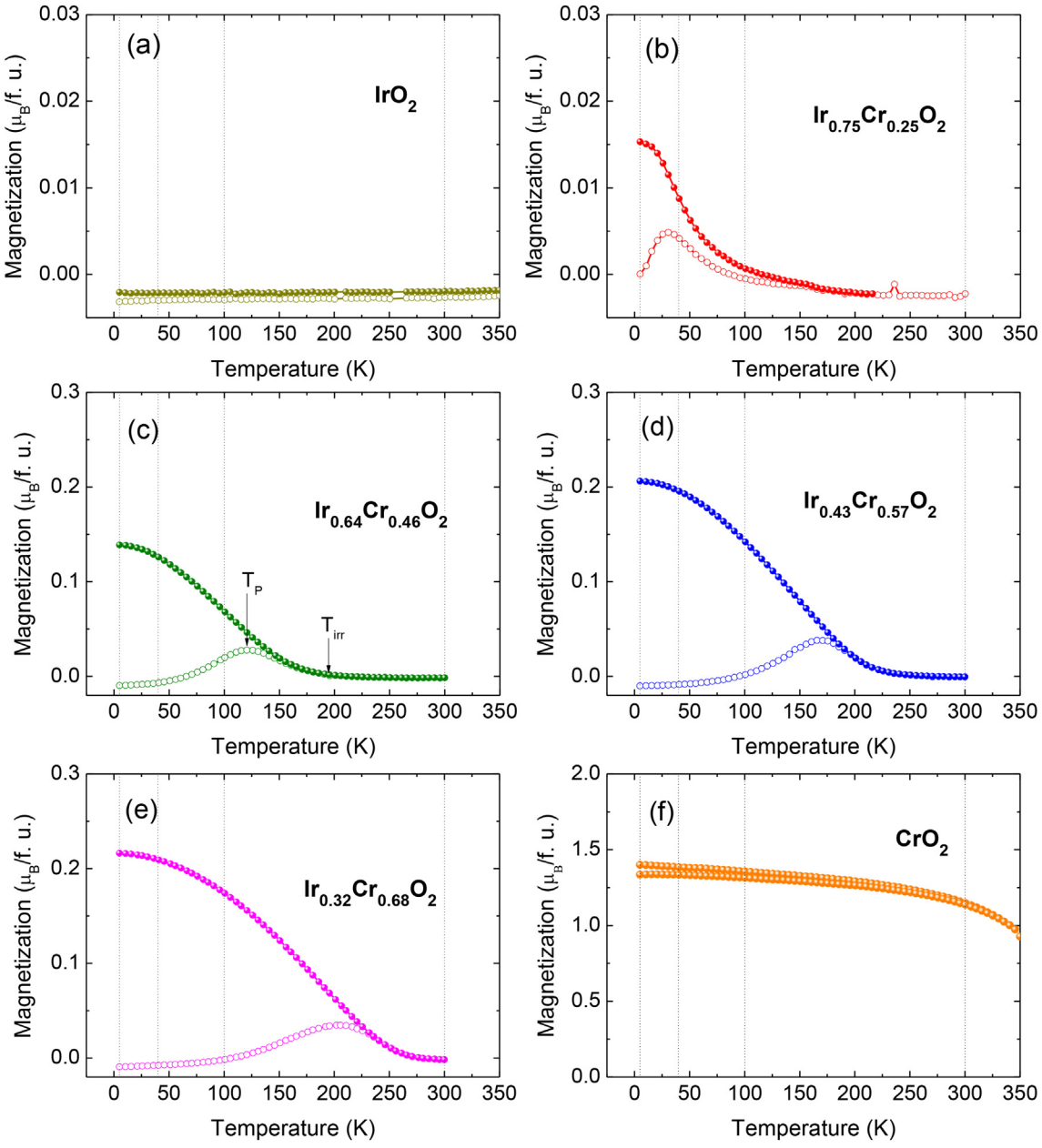

Fig. 5. ZFC (open symbols) and FC (solid symbols) M(T) curves recorded on representative $Ir_{1-x}Cr_xO_2$ samples with an applied field of H = 1 kOe (0.1 kOe for CrO_2).

content is increased as indicated in Fig. 4(b). This points out to an important role of disorder as the underlying mechanism inducing the MIT in $Ir_{1-x}Cr_xO_2$ samples. Additionally, given the large compression of the lattice and the increasing amorphous fraction with Cr doping observed by XRD, structural distortions reducing the bandwidth may also be playing a role in this behavior.

The magnetic behavior of the $Ir_{1-x}Cr_xO_2$ samples largely differs from that of IrO_2 and CrO_2. M(T) curves show a very strong temperature dependence, which also depends on the Cr content (Fig. 5). In all the doped samples the field cooled (FC) magnetization increases with decreasing temperature, while the zero–field cooled (ZFC) magnetization first increases, until T_P, and then decreases monotonically as the temperature decreases. Moreover, a pronounced bifurcation between the FC and ZFC curves occurs at the irreversibility temperature, T_{irr}. The maximum values reached by the FC and ZFC magnetization curves as a function of the Cr content as well as the dependence of T_P are displayed in Fig. 6. In all the cases there is a progressive increase up to $x = 0.68$ followed by a decrease for $x = 0.77$.

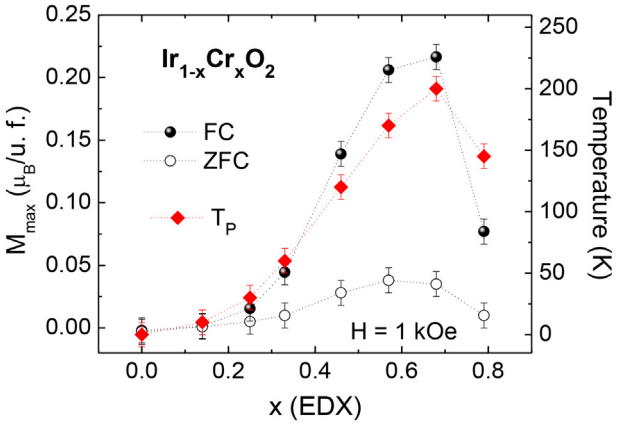

Fig. 6. Maximum magnetization measured in the FC and ZFC curves and evolution of with the Cr content. Dotted lines are guides to the eye.

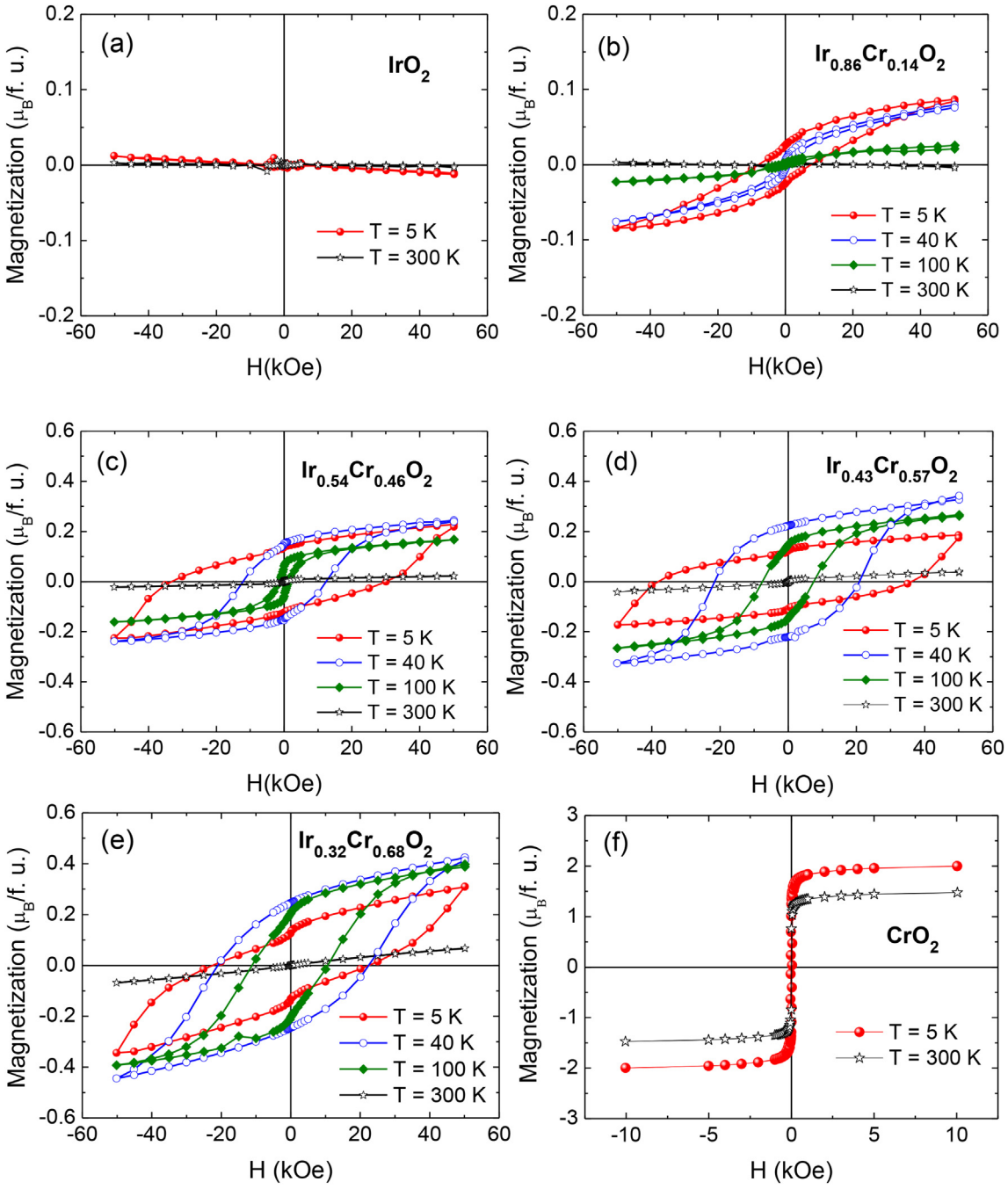

Fig. 7. M(H) curves recorded on representative annealed $Ir_{1-x}Cr_xO_2$ samples at 5, 40, 100 and 300 K. These measurements were done with the field applied in plane. Measurements carried out with the field applied along other directions including out of plane gave similar results.

Accordingly, the behavior of M(H) depends on the temperature (Fig. 7). At RT, a paramagnetic–like behavior is observed in all doped samples, with small magnetization values irrespective of the Cr content. At $T_P < T < T_{irr}$, a ferromagnetic–like component appears in the M (H) curves. The maximum values of magnetization are found to be relatively high and increase with Cr content up to ~0.4 μ_B/f. u. in the $Ir_{0.32}Cr_{0.68}O_2$ sample. It is somehow unexpected that M_{max} decreases for $x = 0.77$. This could be due to the lower crystallinity of this sample observed in the XRD data. Finally, for $T < T_P$ a drastic increase of the coercive field (H_C) is observed. Huge coercive fields, greater than 40 kOe in the $Ir_{0.43}Cr_{0.57}O_2$ film, are observed at $T = 5$ K. It is to be noted that for $0.4 \le x \le 0.8$ the large hysteresis loops are actually minor loops and remain far from saturating up to 50 kOe. This indicates that the actual H_C for these samples is even larger, as well as the magnetic moment. The magnetic response of the ternary $Ir_{1-x}Cr_xO_2$ samples is clearly different from that of pure CrO_2 (Fig. 7(f)), which presents a larger magnetization (~2 μ_B/f. u.) and an almost negligible coercivity ($H_C < 100$ Oe). On the other hand, the results above suggest a scenario where magnetically ordered clusters are formed in the $T_P < T < T_{irr}$ region and an anisotropy source appears at $T < T_P$.

XMCD allows disentangling the magnetic contributions from Ir and Cr atoms. Thus, XMCD spectra were recorded at the Ir $L_{2,3}$ edges and at the Cr K edge on the $Ir_{0.43}Cr_{0.57}O_2$ representative sample. A clear Ir XMCD signal is revealed (Fig. 8(a)). Regarding its temperature and

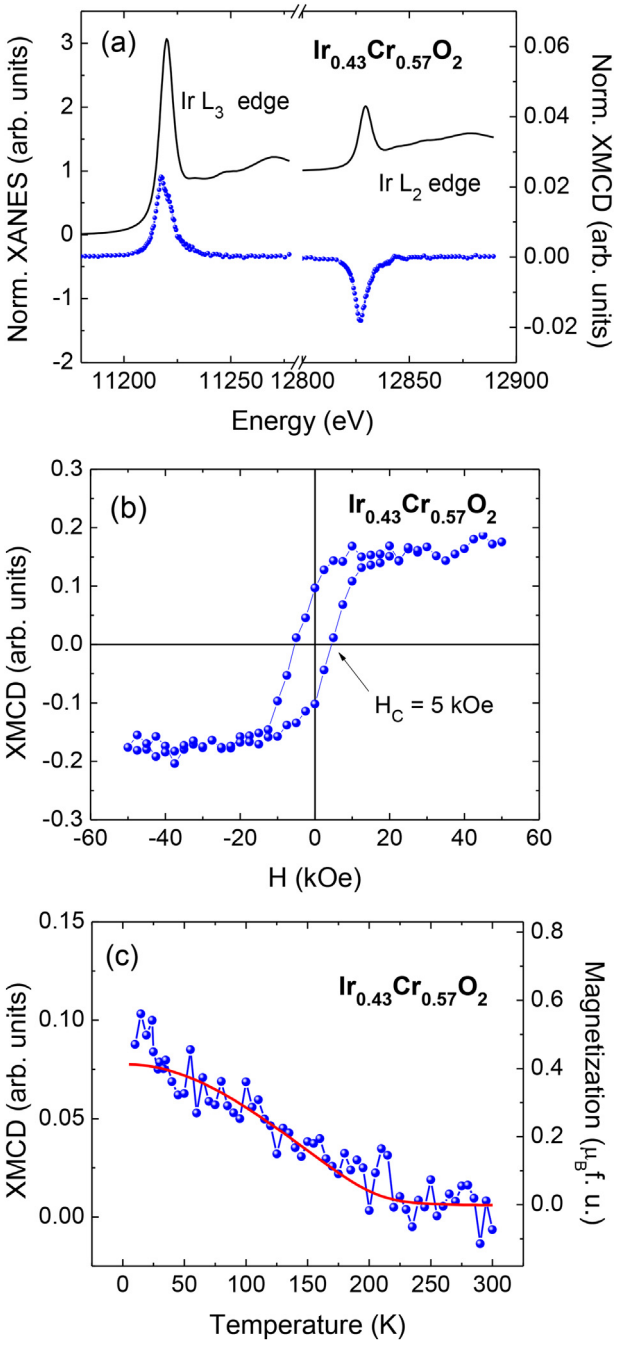

Fig. 8. (a) Normalized XANES and XMCD spectra recorded at the Ir $L_{2,3}$ edges at $T = 10$ K and H = 50 kOe on polycrystalline $Ir_{0.43}Cr_{0.57}O_2$ sample. (b) Ir L_3–edge field–dependent XMCD curve at T = 10 K and $E = 11{,}218$ eV. (c) Ir L_3–edge temperature–dependent XMCD curve with H = 1 kOe. The FC–M(T) is also included for comparison.

field dependence, Fig. 8(b) shows a hysteresis loop with a coercive field $H_C = 5$ kOe and Fig. 8(c) shows that the XMCD(T) curve nicely matches the thermal dependence of the magnetization. The signal in Fig. 8(a) has similar magnitude (~2%) and opposite sign at both absorption edges. This demonstrates an important magnetic contribution of the Ir ions to the magnetic response of the $Ir_{1-x}Cr_xO_2$ films. Sum rule analysis [43,44] indicates that the net magnetic moment of Ir is antiferromagnetically coupled to Cr and basically of spin nature: $m_s \approx -0.11\ \mu_B$/Ir, $m_l = 0.01\ \mu_B$/ Ir. The spin moment value is obtained assuming that the magnetic dipole term T_z is 0. While the precise value depends on the value of T_z, the almost pure spin nature remains invariant. This is q-uite an

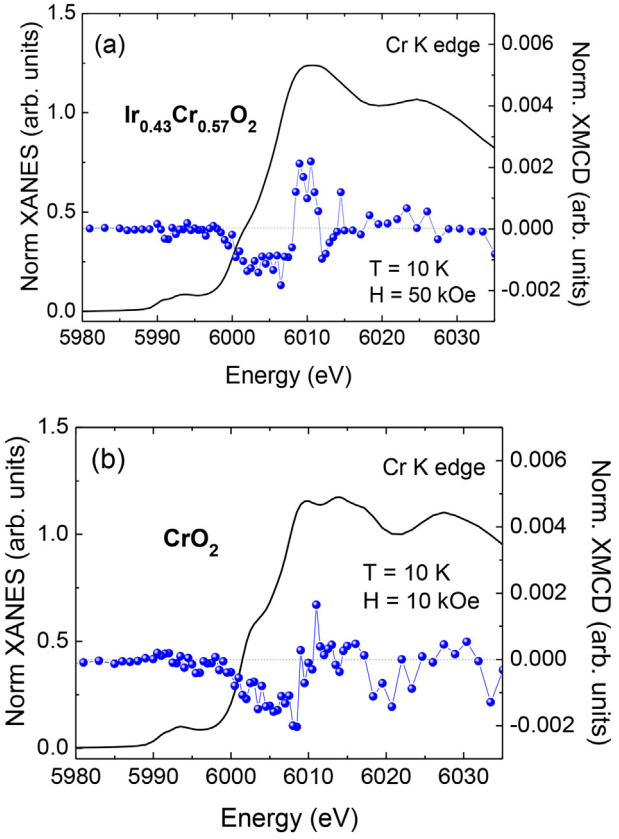

Fig. 9. Normalized XANES and XMCD spectra recorded at the Cr K edge on polycrystalline $Ir_{0.43}Cr_{0.57}O_2$ sample (a) and epitaxial CrO_2 film (b).

unexpected and important result since usually Ir XMCD signals observed in other Ir^{4+} iridates are very small at the L_2 edge, leading to comparable m_s and m_l moments [45–47]. In this case, however, the nature of the magnetic moment is completely different with a drastic quenching of the Ir orbital magnetic moment with $\langle m_l\rangle/\langle m_s\rangle = 0.09$. From this large XMCD the formation of Ir^{5+}, *i.e.* a non–magnetic $J = 0$ ion, is ruled out [48]. This XMCD also discards a $j_{eff} = 1/2$ state for the Ir atoms in these oxides [49]. Since substantial distortions of the IrO_6 octahedra can lead to a quenched orbital moment, one could suggests that the observed quenched $\langle m_l\rangle$ occurs due to Ir^{4+} ions placed in highly distorted IrO_6 octahedra. However, the previously obtained high $\langle \mathbf{L}\cdot\mathbf{S}\rangle$ is difficult to reconcile with a quenched $\langle m_l\rangle$. Otherwise, a Cr–induced magnetic moment should also be considered. While such an origin is frequent in intermetallics and in metallic multilayers through direct orbital overlap [50–52], it is quite controversial in oxides, where just a few cases of neighbor–induced XMCD signals have been only recently reported [53]. If verified, this would be a remarkable result that would clearly tilt the balance in this discussion and would open a new route to engineer the magnetic properties of oxides, thus contributing to future applications.

Fig. 9(a) and (b) show the XMCD spectra recorded at the Cr K edge on the $Ir_{0.43}Cr_{0.57}O_2$ and CrO_2 films, respectively. At first sight both samples show similar XMCD signals. However, the profile of $Ir_{0.43}Cr_{0.57}O_2$ shows an extra feature at 6010 eV that is not observed in CrO_2. While the K–edge is typically used as an indirect probe of the net 3*d* magnetic moment (through 4*p*–3*d* hybridization), the works on intermetallics show that additional contributions due to magnetic neighbor atoms can also be present in the XMCD signal [50]. Based on this one can propose that the low–energy negative peak is Cr–dominated (with 3d character), while the higher energy positive peak can be tentatively associated to Ir contribution. Consequently, the profile

difference observed in this case advises us against inferring magnetic information based on the comparison of the two K–edge signals. Therefore, the currently available Cr XMCD data are not enough to obtain information about the net magnetization of the Cr sublattice. Further work is required in order to clarify the correct interpretation of this signal. In this sense, it is worth noticing the scientific interest of confirming the possible contribution of the Ir neighbors to the Cr XMCD signal as it would be the first experimental evidence of simultaneous observation of two sublattice magnetization at the K–edge XMCD of an oxide.

Therefore, the synthesis and characterization of novel $Ir_{1-x}Cr_xO_2$ samples have so far revealed an interesting, yet intriguing scenario. Compared to CrO_2, the ternary oxides present huge coercive fields. While further and extensive work is needed to completely clarify the origin of this coercivity, some preliminary analysis can already be done at this point. The presence of antiferromagnetic Cr_2O_3 (or Cr^{3+} in any other oxide form) is neither observed in the XRD nor in the XANES measurements. In addition, negligible H_C in Cr_2O_3/CrO_2 nanoparticles and nanorods have been previously reported [54,55]. Hence, an origin associated to the presence of Cr_2O_3 can be reasonably discarded. Similarly, Cr–doped rutile TiO_2 has also proven to show negligible H_C [56]. Likewise, inter–cluster RKKY or dipolar exchange interactions are too weak to be (solely) responsible for the huge coercivity, so stronger short–range interactions should be considered.

Otherwise, one may propose Ir as a key ingredient. Two different pictures can be envisaged. One can propose the high SOC of Ir to be at the origin of the huge H_C in a similar manner to that proposed in $BaIrO_3$ and Sr_3NiIrO_6 [22,23,57]. According to these works the huge H_C would be linked to the unusual spin–orbit–entangled local state of the Ir^{4+} ion and its potential for anisotropic exchange interactions. Alternatively, one can propose an exchange coupled core–shell–like heterostructure where the structural disorder at the surface (shell) of the cluster gives rise to a spin glass behavior that blocks the magnetic response of the whole cluster in a similar way to that observed in Fe_2O_3 nanoparticles [58]. In this picture the antiparallel coupling between Cr and Ir would be a key factor to explain the spin glass behavior of the shell. Both pictures, however, have also some drawbacks. In particular, the small orbital magnetic moment of Ir and the smaller H_C found in the Ir L_3–edge XMCD hysteresis loop do not seem to agree well with an Ir–induced anisotropy.

4. Conclusions

$Ir_{1-x}Cr_xO_2$ ($0.1 < x < 0.8$) rutile phases have been successfully grown for the first time. In particular, polycrystalline $Ir_{1-x}Cr_xO_2$ ($0.1 < x < 0.8$) thin films of ~80 nm have deposited by reactive magnetron co–sputtering followed by an annealing treatment at 600 °C. This provides an alternative method to grow the thermally unstable CrO_2 structure. The structural characterization shows that a rutile single phase is formed in all the samples, confirming that Ir and Cr form a substitutional solid solution phase.

The analysis of the XANES spectra of the $Ir_{0.43}Cr_{0.57}O_2$ sample reveals large 5*d* SOC and confirms the oxidation state of both, Ir and Cr, to be 4+. XMCD shows that Ir has a sizable magnetic moment, $m = 0.10\ \mu_B$/Ir. Surprisingly enough for a Ir^{4+}–iridate, the orbital contribution to the magnetic moment is negligible. These data so far suggest that the magnetic moment of Ir is induced by Cr. This is a remarkable result for an oxide since it can open a new route to engineer the magnetic properties of oxides, thus contributing to future applications.

The electrical and magnetic properties are found to be rather surprising: in contrast to the metallic ground state of IrO_2 and CrO_2, the electrical characterization of the $Ir_{1-x}Cr_xO_2$ samples reveals a semiconductor–like response at low temperature. In addition, contrary to CrO_2, the $Ir_{1-x}Cr_xO_2$ samples present giant coercive fields (greater than 40 kOe). Moreover, it is found that by changing the Cr content, both the magnetization and the coercive field can be widely tuned. These results suggest that the presence of Ir is at the origin of this giant coercivity.

From the applied point of view, the tunability of the magnetic response by dilution provides a route to obtain permanent magnets with designed magnetic hardness. Besides, the $Ir_{1-x}Cr_xO_2$ system presents a huge potential of in spintronics as it combines a half metal with the high SOC required for spin–current to charge–current conversion.

Data availability

The raw/processed data required to reproduce these findings cannot be shared at this time as the data also forms part of an ongoing study.

Declaration of Competing Interest

The authors declare no competing interests.

Acknowledgments

This work was partially supported by the Spanish Ministry of Science and Innovation under contract projects MAT2014–54425–R and MAT2017–83468–R. The authors would like to acknowledge the use of Servicio General de Apoyo a la Investigación–SAI, Universidad de Zaragoza. This research used resources of the APS, a US Department of Energy (DOE) Office of Science User Facility operated for the DOE Office of Science by Argonne National Laboratory under Contract No. DE–AC02–06CH11357. E.A.–E. acknowledges the Spanish MINECO and the European Social Fund for a FPI (Formación de Personal Investigador, 2015) grant.

References

[1] J.M.D. Coey, M. Venkatesan, Half-metallic ferromagnetism: example of CrO2, J. Appl. Phys. 91 (2002) 8345–8350.
[2] S.M. Watt, S. Wirth, S. von Molnár, A. Barry, J.M.D. Coey, Evidence for two-band magnetotransport in half-metallic chromium dioxide, Phys. Rev. B 61 (2000) 9621–9628.
[3] C. Aguilera, J.C. González, A. Borrás, D. Margineda, J.M. González, A.R. González-Elipe, J.P. Espinós, Preparation and characterization of CrO2 films by low pressure chemical vapor deposition from CrO3, Thin Solid Films 539 (2013) 1–11.
[4] X.L. Wang, P.Z. Si, H.L. Ge, K.P. Shinde, K.C. Chung, C.J. Choi, Synthesis, structure and magnetic properties of ultra-high purity CrO2 prepared under high O2-gas pressure, Solid State Sci. 67 (2017) 72–75.
[5] J.S. Parker, S.M. Watts, P.G. Inanov, P. Xiong, Spin polarization of CrO2 at and across an Artificial Barrier, Phys. Rev. Lett. 88 (2002) 196601.
[6] R.S. Keizer, S.T. Goennenwein, T.M. Klapwijk, G. Miao, G. Xiao, A. Gupta, A spin triplet supercurrent through the half-metallic ferromagnet CrO2, Nature 439 (2006) 825–827.
[7] J. Han, J. Shen, G. Gao, CrO2-based heterostructure and magnetic tunnel junction: perfect spin filtering effect, spin diode effect and high tunnel magnetoresistance, RSC Adv. 9 (2019) 3550–3557.
[8] S. Choudhary, P. Mishra, R. Goyal, First-principles study of spin transport in BN doped CrO2–graphene–CrO2 magnetic tunnel junction, Phys. Lett. A 380 (2016) 1098–1101.
[9] X.-Y. Zhang, Y. Chen, Z.-Y. Li, V.G. Harris, Tailoring large magnetodielectric response in core/shell CrO2/Cr2O3 nano-rods, J. Alloys Compd. 692 (2017) 950–954.
[10] X. Deng, Z. Li, Intrinsic ultra-wide completely spin-polarized state realized in a new CrO2 monolayer, Phys. Chem. Chem. Phys. 22 (2020) 17038–17041 (Just accepted).
[11] R. Cheng, B. Xu, C.N. Borca, A. Sokolov, C.-S. Yang, L. Yuan, S.-H. Liou, B. Doudin, P.A. Dowben, Characterization of the native Cr2O3 oxide surface of CrO2, Appl. Phys. Lett. 79 (2001) 3122–3124.
[12] G.P. Singh, S. Ram, J. Eckert, H.J. Fecht, Synthesis and morphological stability in CrO2 single crystals of a half-metallic ferromagnetic compound, J. Phys. Conf. Ser. 144 (2009) 012110.
[13] J. Lu, K.G. West, S.A. Wolf, Novel magnetic oxide thin films, in: Ramanathan (Ed.), Thin Film Metal-Oxide Fundamental and Applications in Electronics and Energy, Springer, 2010.
[14] Ming Cheng, Zhenhua Zhang, Zhihong Lu, Shuo Liu, Ziyang Yu, Changwei Chen, Yuting Li, Yong Liu, et al., Magnetic properties and thermal stability of N-doped CrO2 (100) films, Ceram. Int. 44 (2018) 9664–9670.
[15] Z. Zhang, M. Cheng, Z. Lu, Z. Yu, S. Liu, R. Liang, Y. Liu, J. Shi, R. Xiong, Magnetic properties and thermal stability of Ti-doped CrO2 films, J. Magn. Magn. Mater. 451 (2018) 572–576.

[16] J. Nichols, X. Gao, S. Lee, T.L. Meyer, J.W. Freeland, V. Lauter, D. Yi, J. Liu, D. Haskel, J.R. Petrie, et al., Emerging magnetism and anomalous hall effect in iridate-manganite heterostructures, Nat. Commun. 7 (2016) 12721.
[17] A. Hernando, P. Crespo, M.A. García, Origin of orbital ferromagnetism and giant magnetic anisotropy at the nanoscale, Phys. Rev. Lett. 96 (2006) 057206.
[18] D. Yi, Jian Liu, S.-L. Hsu, L. Zhang, et al., Atomic-scale control of magnetic anisotropy via novel spin-orbit coupling effect in La2/3Sr1/3MnO3/SrIrO3 superlattices, PNAS 113 (2016) 6397–6402.
[19] A. Singh, S. Mohapatra, C. Bhandari, S. Satpathy, Spin-orbit coupling induced magnetic anisotropy and large spin wave gap in NaOsO3, J. Phys. Commun. 2 (2018) 115016.
[20] X. Ma, P. He, L. Ma, G.-Y. Guo, H. Zhao, S. Zhou, G. Lupke, Spin-orbit interaction tuning of perpendicular magnetic anisotropy in L10 FePdPt films, Appl. Phys. Lett. 104 (2014) 192402.
[21] J. Ieda, S.E. Barnes, S. Maekawa, Magnetic anisotropy by Rashba spin–orbit coupling in antiferromagnetic thin films, J. Phys. Soc. Jpn. 87 (2018), 053703.
[22] J. Singleton, J.W. Kim, C.V. Topping, et al., Magnetic properties of Sr3NiIrO6 and Sr3CoIrO6: magnetic hysteresis with coercive fields of up to 55 T, Phys. Rev. B 94 (2016) 224408.
[23] T. Kida, S. Yoshii, M. Hagiwara, T. Nakano, I. Terasaki, Nanoscale spin-dependent transport in a weak itinerant ferromagnet BaIrO3, J. Phys. Conf. Ser. 150 (2009), 022037.
[24] S. Hirosawa, M. Nishino, S. Miyashita, Perspectives for high-performance permanentmagnets: applications, coercivity, and new materials, Adv. Nat. Sci. Nanosci. Nanotechnol. 8 (2017), 013002.
[25] Microwave Materials, Applications Eds, M.T. Sebastian, R.Ubic and H. Jantunen, Wiley, 2017.
[26] K. Fujiwara, Y. Fukuma, J. Matsuno, H. Idzuchi, Y. Niimi, Y. Otani, H. Takagi, 5d iridium oxide as a material for spin-current detection, Nat. Commun. 4 (2013) 2893.
[27] S.K. Panda, S. Bhowal, A. Delin, O. Eriksson, I. Dasgupta, Effect of spin orbit coupling and Hubbard U on the electronic structure of IrO2, Phys. Rev. B 89 (2014) 155102.
[28] X. Ming, K. Yamauchi, T. Oguchi, S. Picozzi, Spin-Orbit Semimetal SrIrO3in the Two-Dimensional Limit, (arXiv preprint) arXiv:1702.04408 2017.
[29] J.M. Kahk, C.G. Poll, F.E. Oropeza, et al., Understanding the electronic structure of IrO2 using hard-X-ray photoelectron spectroscopy and density-functional theory, Phys. Rev. Lett. 112 (2014) 117601.
[30] E. Oakton, D. Lebedev, M. Povia, D.F. Abbott, E. Fabbri, A. Fedorov, et al., IrO2-TiO2: a high-surface-area, active, and stable electrocatalyst for the oxygen evolution reaction, Catal. 7 (2017) 2346–2352.
[31] J. Lim, D. Park, S.S. Jeon, C.-W. Roh, et al., Ultrathin IrO2 nanoneedles for electrochemical water oxidation, Adv. Funct. Mater. 28 (2018) 1704796.
[32] C.R. Natoli, D.K. Misemer, S. Doniach, F.W. Kutzler, First-principles calculation of x-ray absorption-edge structure in molecular clusters, Phys. Rev. A 22 (1980) 1104–1108.
[33] M. Benfatto, S.D. Longa, Geometrical fitting of experimental XANES spectra by a full multiple-scatteringprocedure, J. Synchrotron Radiat. 8 (4) (2001) 1087–1094.
[34] J. Chaboy, Relationship between the structural distortion and the Mn electronic state in La1-xCaxMnO3: a Mn K-edge XANES study, J. Synchrotron Radiat. 16 (2009) 533–544.
[35] G. van der Laan, B.T. Thole, Local probe for spin-orbit interaction, Phys. Rev. Lett. 60 (1988) 1977–1980.
[36] M.A. Laguna-Marco, D. Haskel, N. Souza-Neto, J.C. Lang, V.V. Krishnamurthy, S. Chikara, G. Cao, M. van Veenendaal, Orbital magnetism and spin-orbit effects in the electronic structure of BaIrO3, Phys. Rev. Lett. 105 (2010) 216407.
[37] S. Chikara, G. Fabbris, J. Terzic, G. Cao, D. Khomskii, D. Haskel, Charge partitioning and anomalous hole doping in Rh-doped Sr2IrO4, Pyhys. Rev. B 95 (2017) (060407(R)).
[38] S. Ould-Chikh, O. Proux, P. Afanasiev, L. Khrouz, M.N. Hedhili, D.H. Anjum, M. Harb, C. Geantet, J.M. Basset, E. Puzenat, Photocatalysis with chromium-doped TiO2: bulk and surface doping, ChemSusChem 7 (2014) 1361–1371.
[39] M. Uchida, W. Sano, K.S. Takahashi, T. Koretsune, Y. Kozuka, R. Arita, Y. Tokura, M. Kawasaki, Field-direction control of the type of charge carriers in nonsymmorphic IrO2, Phys. Rev. B 91 (2015) (241119(R)).
[40] J.H. Gruenewald, J. Nichols, J. Terzic, G. Cao, J.W. Brill, S.S.A. Seo, Compressive strain-induced metal–insulator transition in orthorhombic SrIrO3 thin films, J. Mater. Res. 29 (2014) 2491–2496.
[41] G. Bergmann, Weak localization in thin films: a time-of-flight experiment with conduction electrons, Phys. Rep. 107 (1984) 1–58.
[42] F.-X. Wu, J. Zhou, L.Y. Zhang, Y.B. Chen, S.-T. Zhang, Z.-B. Gu, S.-H. Yao, Y.-F. Chen, Metal–insulator transition in SrIrO3 with strong spin–orbit interaction, J. Phys. Condens. Matter 25 (2013) 125604.
[43] B.T. Thole, P. Carra, F. Sette, G. van der Laan, X-ray circular dichroism as a probe of orbital magnetization, Phys. Rev. Lett. 68 (1992) 1943–1946.
[44] P. Carra, B.T. Thole, M. Altarelli, X. Wang, X-ray circular dichroism and local magnetic fields, Phys. Rev. Lett. 70 (1993) 694–697.
[45] D. Haskel, G. Fabbris, M. Zhernenkov, P.P. Kong, C.Q. Jin, G. Cao, M. van Veenendaal, Pressure tuning of the spin-orbit coupled ground state in Sr2IrO4, Phys. Rev. Lett. 109 (2012), 027204.
[46] J.-W. Kim, Y. Choi, S.H. Chun, D. Haskel, D. Yi, R. Ramesh, J. Liu, P.J. Ryan, Controlling entangled spin-orbit coupling of 5d states with interfacial heterostructure engineering, Phys. Rev. B 97 (2018), 094426.
[47] K.S. Pedersen, J. Bendix, A. Tressaud, E. Durand, H. Weihe, Z. Salman, T.J. Morsing, D.N. Woodruff, Y. Lan, W. Wernsdorfer, et al., Iridates from the molecular side, Nat. Commun. 7 (2016) 12195.
[48] M.A. Laguna-Marco, E. Arias-Egido, C. Piquer, V. Cuartero, et al., Magnetism of Ir5+−based double perovskites: unraveling its nature and the influence of structure, Phys. Rev. B 101 (2020), 014449.
[49] B.J. Kim, H. Jin, S.J. Moon, J.-Y. Kim, B.-G. Park, C.S. Leem, J. Yu, T.W. Noh, C. Kim, S.-J. Oh, et al., Novel Jeff=1/2 Mott state induced by relativistic spin-orbit coupling in Sr2IrO4, Phys. Rev. Lett. 101 (2008), 076402.
[50] M.A. Laguna-Marco, C. Piquer, J. Chaboy, X-ray magnetic circular dichroic spectrum at the K edge of the transition metal in R−T intermetallics and its relationship with the magnetism of the rare earth, Phys. Rev. B 80 (2009) 144419.
[51] J. Alonso, M.L. Fdez-Gubieda, G. Sarmiento, J. Chaboy, R. Boada, A.G. Prieto, D. Haskel, M.A. Laguna-Marco, et al., Interfacial magnetic coupling between Fe nanoparticles in Fe–Ag granular alloys, Nanotechnology 23 (2012), 025705.
[52] E. Arias-Egido, M.A. Laguna-Marco, J. Sánchez-Marcos, C. Piquer, J. Chaboy, M. Ávila, J. García López, Microstructural and magnetic characterization of Fe- and Ir-based multilayers, Phys. Rev. Mater. 2 (2018), 014402.
[53] C. Strohm, P. van der Linden, O. Mathon, S. Pascarelli, Simultaneous observation of the Er- and Fe-sublattice magnetization of Ferrimagnetic Er3Fe5O12 in high magnetic fields using XMCD at the Er L2,3 edges, Phys. Rev. Lett. 122 (2019) 127204.
[54] P.Z. Si, X.L. Wang, X.F. Xiao, et al., Structure and magnetic properties of Cr2O3/CrO2 nanoparticles prepared by reactive laser ablation and oxidation under high pressure of oxygen, J. Magn. 20 (2015) 211–214.
[55] A.C. Gandhi, T.Y. Li, T.S. Chan, S.Y. Wu, Short-range correlated magnetic Core-Shell CrO2/Cr2O3 Nanorods: experimental observations and theoretical considerations, Nanomaterials 8 (2018) 312.
[56] S. Larumbe, C. Gómez-Polo, Magnetic properties of N- and (Cr, N)-doped TiO2 nanoparticles, IEEE Trans. Magn. 51 (2015) 1–4.
[57] E. Lefrancois, A.-M. Pradipto, M. Moretti Sala, et al., Anisotropic interactions opposing magnetocrystalline anisotropy in Sr3NiIrO6, Phys. Rev. B 93 (2016) 224401.
[58] J. Sánchez-Marcos, M.A. Laguna-Marco, R. Martínez-Morillas, E. Céspedes, F. Jiménez-Villacorta, N. Menéndez, C. Prieto, Exchange bias in iron oxide nanoclusters, J. Phys. Condens. Matter 23 (2011) 476003.